

Development and Application of a ReaxFF Reactive Force Field for Cerium Oxide/Water Interfaces

Luca Brugnoli, Maria Cristina Menziani, Shingo Urata, and Alfonso Pedone*



Cite This: <https://doi.org/10.1021/acs.jpca.1c04078>



Read Online

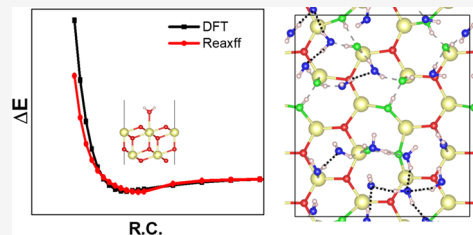
ACCESS |

Metrics & More

Article Recommendations

Supporting Information

ABSTRACT: Ceria (CeO_2) is a well-known catalytic oxide with many environmental, energy production, and industrial applications, most of them involving water as a reactant, byproduct, solvent, or simple spectator. In this work, we parameterized a Ce/O/H ReaxFF for the study of ceria and ceria/water interfaces. The parameters were fitted to an *ab initio* training set obtained at the DFT/PBE0 level, including the structures, cohesive energies, and elastic properties of the crystalline phases Ce, CeO_2 , and Ce_2O_3 ; the O-defective structures and energies of vacancy formation on CeO_2 bulk and CeO_2 (111) surface, as well as the absorption and reaction energies of H_2 and H_2O molecules on CeO_2 (111). The new potential reproduced reasonably well all the fitted properties as well as the relative stabilities of the different ceria surfaces, the oxygen vacancies formation, and the energies and structures of associative and dissociative water molecules on them. Molecular dynamics simulations of the liquid water on the CeO_2 (111) and CeO_2 (100) surfaces were carried out to study the coverage and the mechanism of water dissociation. After equilibration, on average, 35% of surface sites of CeO_2 (111) are hydroxylated whereas 15% of them are saturated with molecular water associatively adsorbed. As for the CeO_2 (100) surface, we observed that water preferentially dissociates covering 90% of the available surface sites in excellent agreement with recent experimental findings.



1. INTRODUCTION

Ceria (CeO_2)-based materials are widely used in various technological fields, primarily in catalytic applications in the environmental, energy, and hydrogen production fields,^{1,2} as abrasives in the glass polishing^{3,4} and as biocompatible materials for medical uses.^{5–7}

All these applications involve either liquid or gaseous water as a reagent, product, solvent, or simply as a moisture influencing (positively or negatively) the final properties and functions of ceria. Therefore, the understanding of the surface chemistry of ceria in contact with water, including the water structure and dynamics on different ceria surfaces, is fundamental to optimize functions and processes for this fascinating oxide.

For these reasons, the interaction of CeO_2 with water has been intensively investigated both experimentally and computationally in the last decades.⁸ X-ray photoelectron spectroscopy (XPS),^{9–12} temperature-programmed desorption (TPD),^{9–12} and scanning force microscopy (SFM)^{11,13} studies revealed that water can adsorb either associatively and/or dissociatively on (111) and (100) ceria surfaces. In addition, other experimental studies have unraveled that water tends to dissociate on the (100) termination^{9,10,12,14–19} and on defective (111) surfaces where oxygen vacancies act as reactive sites.^{10,12} Contrarily, the structural and dynamics details of the ceria–water interfaces, the mechanisms of absorption and dissociation of water, and the possible role of hydrogen bonding (H-bond) patterns have not yet been fully assessed from these experiments.

Computational studies have provided valuable information on this aspect. Most of the simulations of the water/ceria systems have been performed at the density functional theory (DFT) level using periodic surface models. The majority of these investigations focused on the interaction of a single water molecule adsorbing, either associatively or dissociatively, on the ceria surfaces, while a few studies considered multiple water molecules.^{17–32} The (111) ceria surface has attracted more interest²¹ since it is the most thermodynamically stable and experimentally characterized.⁸ As summarized in ref³³ on the stoichiometric surfaces, the associative and dissociative adsorption energies of water calculated by the DFT range from –0.3 to –0.7 eV, depending on the surface coverage of water layers, conformation of the water, and slab thickness or the functional used.³⁴

When multiple water molecules (a coverage of 1.0 monolayer (ML) or more) interact with ceria surface, the partial dissociation of water was found to be energetically favorable.³⁴ This is in agreement with *ab initio* molecular dynamics simulations of liquid water on CeO_2 (111), which

Received: May 7, 2021

Revised: June 11, 2021

demonstrated that about 20% of the adsorbed water is dissociated at room temperature.³⁰

Although all these computational studies have provided fundamental insights on the ceria–water interactions, the expensive computational cost of DFT calculations severely limit the model size up to a few hundreds of atoms and simulation time of *ab initio* DFT molecular dynamics (MD) simulations to a few picoseconds.

A possible alternative to alleviate the size and time limitations is to resort to the reactive force field (ReaxFF) model proposed by van Duin et al.,^{35,36} which can describe the bond breaking and thus chemical reactions in different environments more efficiently than DFT calculations (even though with a less accuracy), enabling one to investigate ceria–water interactions using much larger model systems for longer timescales, as it has been done for other oxides.^{37–40}

In the ReaxFF model, the atom connectivity of the systems and atomic charges are not pre-determined as in conventional classical force fields for biomolecules.⁴¹ Both the bond and valence angle energies smoothly depend on the bond order calculated between two species, allowing the breaking and formation of chemical bonds. The atomic charges needed to compute the Coulombic interactions are updated at each time step of the simulation by employing the electronegativity equalization method,⁴² allowing charge redistributions and possibly mimicking charge transfers albeit with some weaknesses in the dissociation limit.⁴³

A drawback of this model that hampers its application to complex multicomponent systems relies in the lack of accurate parameters suitable to study a multitude of materials. Two major difficulties to obtain a suitable and accurate parameter set are (i) the ReaxFF is composed of a variety of energy terms each containing multiple parameters, which makes parameters optimization not trivial; (ii) it requires a large number of computationally expensive quantum mechanical calculations as a training dataset.

So far, a parameter set of the ReaxFF for Ce–O interaction was developed⁴⁴ and used to model the bulk, surfaces, nanoparticles, O-defective systems of ceria, the Pd–ceria interface, and the adsorption of fluorinated alkanes on ceria.^{45–47} However, this parameterization fails to simulate the dynamics of defects in the bulk ceria⁴⁴ and, since the Ce–O–H interactions have not been included, it is not suitable for investigating ceria–water systems. Moreover, the current parameterization is not transferable because the parameters for water oxygen in the general ReaxFF are different from that used for ceria oxygen.⁴⁸

To overcome these limitations of the current ReaxFF parameters for Ce–O systems, we, for the first time, have developed a new set of Ce–O–H parameters based on hybrid DFT calculations and applied them to investigate the structure and dynamics of gaseous and liquid water on (111) and (100) ceria surfaces.

The manuscript is organized as it follows: in the next section, the DFT calculations used to generate the training dataset, the fitting strategy, and the MD settings used to study the dynamics of ceria–water interfaces are described. The results have been validated against our own and literature QM data using static calculations. In the last section, the new ReaxFF parameter set has been applied to study, by means of MD simulations, how liquid water molecules interact with the (111) and (100) surfaces.

2. COMPUTATIONAL METHODS

2.1. The Training Dataset. As training data, we mainly used the properties computed on different ceria systems by means of accurate hybrid DFT calculations exploiting the PBE0⁴⁹ functional, while several experimental data were also considered in the cases of not reliable DFT calculations. The theoretical training data includes (1) structural and elastic properties of CeO_2 and Ce_2O_3 , (2) the structure of stoichiometric and defective CeO_2 (111) surfaces, and (3) the structure and binding energy of a single water molecule associatively and dissociatively adsorbed on the ceria (111) surface. The potential energy surface (PES) of the diffusion of oxygen along the (111) surface and H_2 oxidation on the stoichiometric CeO_2 surface were also considered in the training set. The experimental training set includes (1) structural and elastic properties of the bulk γ -Ce and (2) the cohesive energies of bulk γ -Ce, CeO_2 , and Ce_2O_3 , which are not well reproduced by the DFT calculations.

To evaluate properties related to the formation of oxygen vacancies, a supercell $2 \times 2 \times 2$ of bulk ($\text{Ce}_{32}\text{O}_{64}$) and a supercell 2×2 of (111) surface with 9 atomic layers ($\text{Ce}_{12}\text{O}_{24}$) were modeled. Moreover, two defect configurations were considered: one located in the first atomic layer and the other one located on the third layer.

As in the previous study by Broqvist *et al.*,⁴⁴ the available experimental data of the metallic phases of cerium was considered because the DFT calculation is inaccurate for the system. Note that, contrary to the previous work, we considered the γ -phase instead of the α -phase⁴⁴ since reliable experimental data of the elastic constants are available.^{50,51} For the same reason, the experimental cohesive energies derived from the respective heat of formation of CeO_2 and Ce_2O_3 were used.⁵²

Instead of the volume-energy equation of state of the CeO_2 and Ce_2O_3 bulk phases, we considered the elastic properties since they provide reliable information of the potential energy surface along different deformation directions.

To model the Ce/O/H interactions, structures optimized by DFT calculations of H_2 and H_2O adsorbed on the stoichiometric CeO_2 (111) surface were considered by adopting the same slab model used for the surface defects. To determine water-related parameters, both associative and dissociative water molecules were considered. Moreover, the minimum energy path (MEP) from the associative to dissociative forms of the adsorbed water along the (111) surface was included in the training data.

2.2. DFT Calculations. Periodic DFT calculations were performed using the CRYSTAL17⁵³ code with atom-centered Gaussian functions as basis sets, which allows us to employ hybrid functionals for reducing the computational costs compared to plane-waves based quantum mechanics (QM) codes. The global hybrid PBE0 functional was used since it well reproduces the properties of bulk and surfaces of ceria oxides (CeO_2 , Ce_2O_3 , and reduced-phases CeO_{2-x}) without using empirical corrective parameters, as confirmed in previous works.^{54–60} Spin polarization was considered only for the systems containing Ce^{3+} and in those cases only the high spin solutions (ferromagnetic) were employed.

Dispersion interactions were not included in the training set since their inclusion through the Grimme's dispersion correction D2⁶¹ was shown to have a negligible effect on the adsorption energy, conformation geometries, and relative

stabilities of water on ceria surfaces.³¹ Following to our previous works, two distinct basis sets were used.^{59,62,63} The less extensive BS1 basis set was used for geometry optimization, except for the bulk CeO₂ and Ce₂O₃ models to which the BS2 basis set was used. The more extensive BS2 basis set was employed to compute energies of the models optimized with the BS1 basis set and elastic properties of bulk cerium oxides. For both basis sets, the inner core of Ce was described by a semi-relativistic effective core potentials (ECP),⁶⁴ while the 4s²4p⁶5s²4d¹⁰5p⁶6s²5d¹4f¹ valence electrons were treated with a [10sp8d8f]/[4sp3d3f] contraction scheme in BS1 and the larger [12s12p9d8f]/[8s7p4d4f] one in BS2. The oxygen atoms of oxide and molecular species have been treated differently in BS1: a modified 8-411G(d) basis set with re-optimized exponents⁶⁵ and a larger [13s7p2d4f]/[7s4p7p2df] contraction scheme were used for oxygen in oxide, O₂, and H₂O, respectively. In the latter case, all primitives with exponents below 0.1 were removed from the original basis set⁶⁶ to avoid pseudo-linear dependency issues. In BS2, instead, the [13s7p2d4f]/[7s4p7p2df] contraction scheme has been used for all the oxygen. In all cases, a POBTZVP all-electron basis set was applied to H.⁶⁷

As done in a previous benchmarking investigation,⁵⁹ we used a Monkhorst-Pack grid⁶⁸ 6 × 6 × 6 for geometry optimization and an augmented grid 12 × 12 × 12 for the elastic properties computation. Calculations at the Γ point were retained sufficient for the optimization of the CeO₂ supercell 2 × 2 × 2 with the vacancy. Finally, a k-point mesh of 4 × 4 × 1 was adopted for the 2D surface models of CeO₂ (111), (110), and (100). The radial and angular points for the integration grid were generated according to the Gauss-Legendre radial quadrature and Lebedev two-dimensional angular point distribution schemes.⁶⁹ The default grid (XLGRID) was employed for all calculations.

The truncation criteria for bielectronic integrals of the Coulomb and exchange infinite lattice series were controlled by five thresholds (ITOL1, ITOL2, ITOL3, ITOL4, and ITOL5), which were set to 8 (ITOL1-ITOL4) and 20 (ITOL5) for all the calculations.⁷⁰ The structures were judged to be optimized when the maximum atomic gradient and maximum atomic displacement were simultaneously below 0.00045 Hartree/Bohr and 0.001200 Bohr, respectively.

2.3. The ReaxFF Reactive Force-Field Method. Since the detailed theoretical description of the ReaxFF methods can be found in the works by van Duin and coworkers,^{35,36} we here report only a short description. The total energy of the systems E_{tot} in the force field is computed as a sum of contributions given by the equation

$$\begin{aligned} E_{\text{tot}} = & E_{\text{bond}} + E_{\text{val}} + E_{\text{tors}} + E_{\text{over}} + E_{\text{under}} + E_{\text{lp}} \\ & + E_{\text{vdwals}} + E_{\text{coulomb}} \end{aligned} \quad (1)$$

The individual contributions correspond respectively to the bond energy (E_{bond}), the valence angle energy (E_{val}), the torsion-angle energy (E_{tors}), the overcoordination penalty energy (E_{over}), the undercoordination penalty energy (E_{under}), the lone pair energy (E_{lp}) and finally the nonbonding terms, the van der Waals (E_{vdwals}), and Coulombic energies (E_{coulomb}). Apart from the nonbonding terms, all the others are bond-order-dependent, i.e., they depend on the local environment of each atom: the bond order is computed from the interatomic distances and the atoms coordination, and it varies at each step of the simulation. The Coulomb contribution is derived from

the atomic charges, which are dynamically computed with the electronegativity equalization method (EEM),⁴² which allows the redistribution of the charges with the evolution of the system geometry. The van der Waals term includes the short-range Pauli repulsion and the long-range dispersion. Both the bonding and non-bonding terms are screened by a taper function to avoid discontinuities and an excessive repulsion at short distances, respectively.

2.4. Parameter Fitting Strategy. The fitting of the potential parameters was performed by using the GULP code.^{71,72} The parameter optimization procedure is intended to minimize an error function F defined as

$$F = \sum_{i=1}^M w_i (f_{i,\text{obs}} - f_{i,\text{cal}})^2 \quad (2)$$

where M is the total number of observables, w_i is a weighting factor for each observable, and $f_{i,\text{obs}}$ and $f_{i,\text{cal}}$ are training data (the experimental or QM-computed values) and calculated values by an obtained parameter set, respectively. In this work, we adopted the BFGS minimization algorithm⁷³ to minimize the error function F .

With the exception of the potential energy surfaces corresponding to the H₂ adsorption and the MEP for H₂ and H₂O dissociation, the fitting procedure was performed using the relaxed fitting algorithm: the least squares objective function was computed on the basis of the changes in structure during optimization, rather than the forces/stresses at the experimental/QM configuration.⁷⁴

We started from the parameters developed by Broqvist *et al.*⁴⁴ and re-optimized the Ce/O parameters on the properties of cerium oxides. Afterward, the parameterization of the Ce/H and Ce/O/H terms were performed on the basis of ceria–water and ceria–hydrogen/oxygen systems, as described above, using as starting values of the parameters developed for Zr/H and Zr/O/H.^{75,76} The atomic parameters of O and H were taken from the latest model for water⁴⁸ and kept fixed during the optimization.

Each parameter was fitted one by one, starting from the atomic parameters of the Ce, following with the two body terms Ce–Ce, Ce–O, and the angle terms Ce–O–Ce, O–Ce–O, O–O–Ce, and Ce–Ce–O were determined. The procedure was repeated for several cycles by changing the weights associated to the different observables in order to tailor the fitting procedure. The weights were chosen in such a way that all the observables considered in the parameterization contribute to a comparable extent to the final penalty function while at the same time avoiding numerical instabilities. The force-field parameters can be found in the GULP input file reported in the Supporting Information.

After obtaining a satisfactory accurate parameter set for atomic Ce and the two body Ce–Ce interactions to reproduce the training data related to the γ -Ce, these parameters were kept constant during the refinement of two- and three-body parameters for Ce–O, which was optimized to reproduce the training dataset for the bulk and surfaces of cerium oxides without water molecules.

Subsequently, parameters for the two body Ce–H terms and of the tree-body Ce–O–H terms were determined to reproduce the training dataset for the ceria–water systems: the binding energy of associative and dissociative water molecules and the PESs of H₂ oxidation on the (111) CeO₂ surface. Once a reliable parameter set of the Ce–O–H was

obtained, a final refinement was carried out by considering all the structures and observables of the training dataset. The optimization flow is shown in Figure 1.

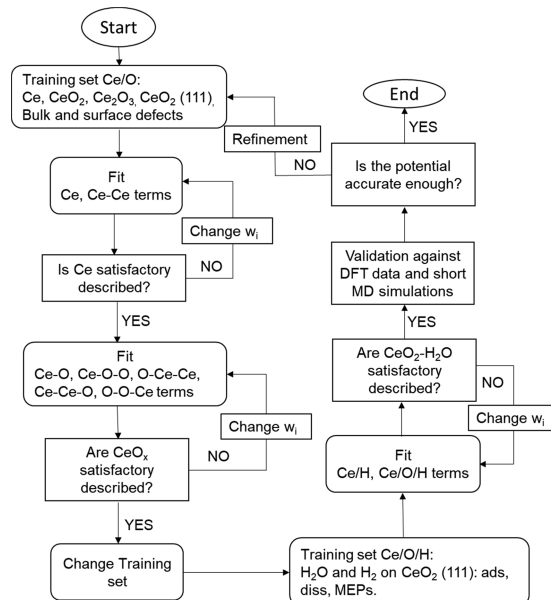


Figure 1. Flow chart representing the route adopted in the fitting of the Ce/O and of the Ce/O/H potential.

2.5. MD Simulation. All the static and dynamical calculations with the ReaxFF were performed using the software GULP^{71,72} (version 5.2). The static geometry optimizations were performed with the conjugate gradient algorithm, and the convergence thresholds for both the gradient and displacement are 1.0×10^{-4} . The MD simulations were performed in the canonical (NVT) ensemble. The velocity Verlet scheme was employed to integrate the equation of motion with a time step of 0.1 fs.⁷⁷ The constant temperature of the system was imposed by a Nosé–Hoover thermostat with a relaxation time of 100 fs.⁷⁸ A seventh degree tampering polynomial scheme of the bond order was adopted, as implemented in the simulation code, to improve the numerical stability and accuracy of the simulations.⁷⁹

The unit cells of surface slab models were generated by cutting bulk CeO₂ with a lattice constant of $a = 5.42 \text{ \AA}$ in (111) and (100) orientation, respectively. Supercells p(4 × 4) with 12 atomic layers and c(4 × 4) with 13 atomic layers were used respectively for the (111) and (100) slab models, which account for 64 CeO₂ units and 96 CeO₂ units. The spacing between the periodic images of the slab along the z axis were

chosen to account for 180 and 200 water molecules respectively on the (111) and (100) model, with a density of 1 kg/m³. MD simulations at 300 K were performed on both systems to model the liquid water/cevia interactions. Water desorption was also examined by using MD simulations after removing the cell periodicity along the z axis by heating the systems from 200 to 1400 K with a rate of 0.5 K/ps.

3. RESULTS AND DISCUSSION

In this section, we discuss the performance of new ReaxFF parameterization in reproducing several observables for the ceria and ceria/water systems. The outline is as follow: Section 3.1 reports the performance of the new ReaxFF on the bulk properties of metallic Ce allotropes, CeO₂, and Ce₂O₃ (see Figure 2), Section 3.2 deals with the oxygen vacancies on the bulk CeO₂ and on the surface (111), Section 3.3 reports the results for the interaction of H₂ and H₂O with the surface (111), and finally, Section 3.4 reports the results of the MD simulations of water on the surfaces (111) and (100).

3.1. Bulk Properties. 3.1.1. *Ce.* As mentioned in the previous section, due to the inaccuracy of the DFT calculation in describing the Ce polymorphs, the experimental data values were used as reference. Moreover, the γ -phase was considered due to the availability of the experimental data, such as elastic constants, bulk modulus, shear modulus, and Young's modulus, structural parameters, and cohesive energies.^{50,51} The comparison between the experimental and computational values is presented in Table 1. Even though a relatively large error is found for the Young's modulus (30%), the other properties including the lattice constant and the cohesive energies were reproduced rather well (within 7% for the cohesive energy and within 1% for the other properties). The potential was also tested on other Ce allotropes: α , β , and δ . The results also reported on Table 1 show that the lattice parameters were well reproduced within 1% of deviation from the experimental values, except for the α -Ce, which is isostructural with the γ -phase. The δ phase, stable at high temperatures, has the highest cohesive energies −3.974 eV, while β -Ce and γ -Ce have almost the same cohesive energies, −4.0024(0) and −4.0023(7) eV, respectively, in agreement with the phase diagram of these species.

3.1.2. *CeO₂.* Table 2 reports the calculated bulk properties of the fluorite-like structure of CeO₂, compared with the ones obtained by DFT calculations and the experimental data. The DFT observables were used in the fitting and are thus very well reproduced (discrepancies within 1–2%) with the exception for the C₄₄ elastic constant. To validate the potential, the results for the rutile polymorph of CeO₂ were also simulated with both DFT and ReaxFF. Table 2 shows that the new potentials reproduce well both the lattice parameters and the

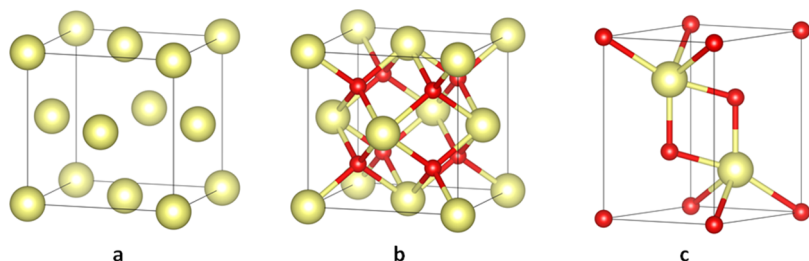


Figure 2. Bulk crystal structures of (a) fcc γ -Ce, (b) fluorite-CeO₂, and (c) A-type Ce₂O₃. Ce and O atoms are respectively light yellow and red colored.

Table 1. Lattice Parameters (a and c), Elastic Properties Available, and Cohesive Energies per Ce Ions (E_{coh}) of the Four Ce Allotropes^{a,b}

phase	crystal structure	a (Å)	c (Å)	B_0 (GPa)	E (GPa)	G (GPa)	E_{coh} (eV)
α -Ce	fcc	5.153 (4.85 ⁸⁵)					-4.0023(7)
β -Ce	dhcp	3.644(3.681 ⁸⁶)	11.902 (11.857)				-4.0024(0)
γ -Ce	fcc	5.153 (5.161 ⁸⁶)					-4.0023(7)
δ -Ce	bcc	4.061 (4.11 ⁸⁷)					-3.9740

^aCe allotropes are ordered according to their stability at an increase in T , at the P of 1 atm. α -Ce is stable up to 150 K, then the β -phase exists up to about 300 K, while the γ -phase is stable from about 250–1000 K. At T above, the δ -Ce forms before reaching the melting point. ^bExperimental data available are reported in parentheses.^{51,84}

Table 2. Comparison of the Fitted, Theoretical, and Experimental Bulk Properties of the Fluorite-CeO₂ Adopted in the Fitting^c

method	a (Å)	c (Å)	B_0 (GPa)	C_{11} (GPa)	C_{12} (GPa)	C_{44} (GPa)	E_{coh} (eV)
ReaxFF	5.420 (4.972)	(3.633)	201.6	392.7	106.0	93.6	-20.92 (-20.04)
PBE0	5.401 (5.097)	(3.585)	209.0	406.9	110.1	60.4	-19.36 (-18.88)
Exp	5.391 ^a		204 ⁸⁸	403 ⁸⁸	105 ⁸⁸	60 ⁸⁸	-20.74 ^b

^aExtrapolated from ref⁸⁹ for 0 K. ^bComputed as in ref⁹⁰ but using ΔH_f (298 K) CeO₂ = -1088.7 kJ/mol.⁸⁴ ^c C_{11} , C_{12} , and C_{44} are the independent component of the elastic tensor. For the meaning of the other observables, see the description of Table 1. Values calculated on the rutile-CeO₂ are in parentheses.

Table 3. Comparison of the Fitted, Theoretical, and Experimental Bulk Properties of the Ce₂O₃ Adopted in the Fitting

method	a (Å)	c (Å)	B_0 (GPa)	C_{11} (GPa)	C_{12} (GPa)	C_{13} (GPa)	C_{33} (GPa)	E_{coh} (eV)
ReaxFF	3.744	6.144	153.8	249.3	153.2	92.6	233.3	-34.79
PBE0	3.880	6.061	136	238	137	94	151	-33.37
Exp	3.891 ⁹¹	6.059 ⁹¹	111 ⁹²					-34.99 ^a

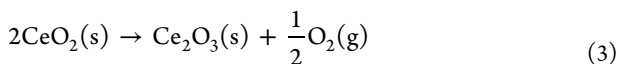
^aComputed as for the E_{coh} of CeO₂, with ΔH_f (298 K) Ce₂O₃ = -1796.2 kJ/mol.⁸⁴

difference between the cohesive energies of the two polymorphs, confirming the fluorite structure as the most stable.

3.1.3. Ce₂O₃. The cerium sesquioxide Ce₂O₃ A-type (Figure 2c) was also adopted for parameter fitting, different from the original parameterization, which has used it only for the validation of the potential.⁴⁴ The same properties for CeO₂ were set to be objective variables for optimization, even though the weights for the elastic properties were lowered by a factor 2. The results are summarized in Table 3.

This phase is fully reduced and deviates from the stoichiometric or partially reduced cerium oxide that this force field mainly aims to describe. However, it is useful to capture the thermochemistry of the Ce⁴⁺/Ce³⁺ redox process that characterizes these materials.

The reaction of reduction of the CeO₂ can be expressed as



The corresponding reduction energy is

$$E_{red} = E_{\text{Ce}_2\text{O}_3} + \frac{1}{2}E_{\text{O}_2} - 2E_{\text{CeO}_2} \quad (4)$$

The new ReaxFF parameterization reproduces fairly well the reaction energy ($E_{red} = 4.5$ eV) with respect to the experimental value ($E_{red} = 4.0$ eV).²⁰ The hybrid DFT PBE0 underestimated it by 1.3 eV, and for this reason, this observable was not used in the fitting. Despite this, PBE0 reproduces remarkably well many others properties of the two oxides.⁵⁹

3.1.4. Partially Reduced Bulk CeO₂. The oxygen vacancy (V_O) in the bulk ceria was modelled by removing an oxygen

atom from the supercell $2 \times 2 \times 2$ of the primitive cell, as stoichiometry Ce₃₂O₆₄ (see Figure 3). The DFT calculations of the defect model were performed to optimize both the atom positions and the cell parameters, which allow lattice expansions associated with the reduction of two Ce⁴⁺ to

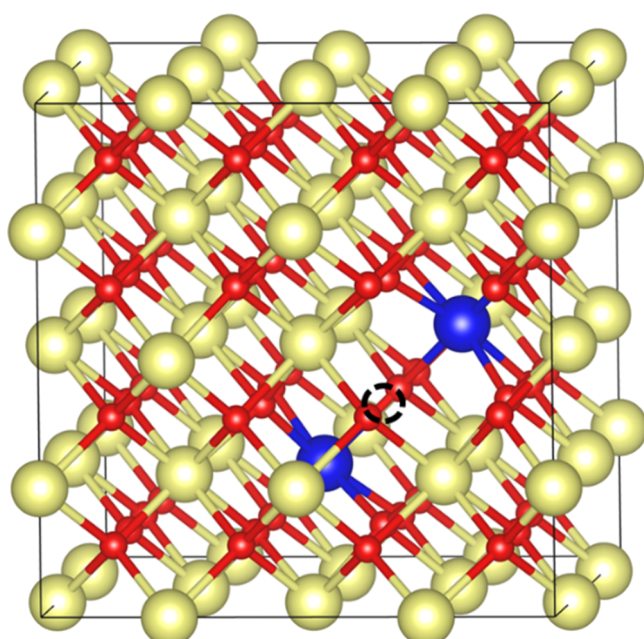
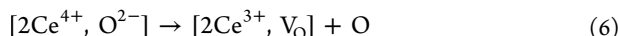
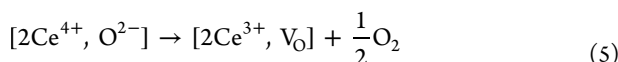


Figure 3. CeO₂ conventional supercell $2 \times 2 \times 2$ with one O vacancy (dotted black circle). In blue are the Ce³⁺ ions formed upon O removal, located in the first coordination shell of the removed O (nearest neighbor configuration).

Ce^{3+} due to the oxygen vacancy. The reaction can be summarized as



These reactions involve the localization of the pair of electrons left in the vacancy into the empty 4f states of the 2 Ce^{4+} ions. It is worth highlighting that the E_{fv} of reaction 5 is computed as

$$E_{\text{fv}} = E_{\text{CeO}_{2-x}} + \frac{1}{2}E_{\text{O}_2} - E_{\text{CeO}_2} \quad (7)$$

where $E_{\text{CeO}_{2-x}}$, E_{O_2} , and E_{CeO_2} are the energies of the reduced ceria, molecular oxygen, and perfect ceria bulk, respectively. This should be remarked to differentiate our results from the ones reported by Broqvist *et al.*,⁴⁴ which adopted an in-cell method where the extracted oxygen molecule was included in the cell.

The computed reaction energies for reactions 5 and 6 differ only for half the bond energy of the O_2 , and the comparison is thus useful to highlight the error associated to the description of the oxygen molecule. In the DFT calculations, of the many possible quasi-degenerate configurations for the Ce^{3+} ions, only the one with both the reduced ions next to the vacancy site was considered being the most straightforward to model.

The DFT method is known to underestimate the energy of formation of the vacancy (E_{fv}) with respect to the experimental measurements;²⁰ therefore, here only the geometry of the optimized defective structure was considered. The comparison between the computed energetics and volume expansion for different methods is reported in Table 4. Although the ReaxFF

Table 4. Energy of Formation of an O Vacancy E_{fv} in the Bulk of CeO_2 and Atomization Energy of the O_2 Molecule, Both Expressed in eV, along with the Cell Volume Expansion ΔV Associated with Respect to the Pristine Cell

method	E_{fv} (1/2 O_2)	$E_{\text{fv}}(\text{O})^a$	E_{atom} $\text{O}-\text{O}$	$\Delta V\%$
ReaxFF (this work)	4.16	6.70	5.08	0.22
ReaxFF ⁴⁴	4.80	7.54	5.48	0.23
PBE0	3.84	6.46	5.37	1.03
PBE+U ($U = 5$) ⁴⁴	3.30	6.40	6.20	
Exp	4.2 ± 0.3^{20}	6.82 ± 3^{20}	5.23 ⁹³	0.30 ^{94b}

^aComputed by adding $1/2E_{\text{atom}}$ $\text{O}-\text{O}$ to E_{fv} (1/2 O_2). ^bInterpolation from the diagram of fig. 6 of ref.⁹⁴ considering a concentration of O vacancies of 1/64.

can describe the reduction of the bulk ceria following the removal of oxygen, the excess of negative charge is distributed evenly among the 4 Ce atoms surrounding the vacancy, thus preventing a clear distinction between Ce^{3+} and Ce^{4+} ions contrary to the PBE0 calculations. Despite this, the computed V_0 formation energy of 4.10 eV is in good agreement with the experimental measurements (4.2 ± 0.3 eV).²⁰ In ceria, the formation of oxygen vacancies is associated with lattice expansion due to the larger radius of the Ce^{3+} ions with respect to the Ce^{4+} and to the repulsion between the cations surrounding the oxygen defect.

The PBE0 calculations found that the volume expansion is 1.08%, while the ReaxFF predicts the dilatation as only 0.22%. The Ce–Ce distance between the 4 cations surrounding the vacancy increases of 6.5% and 6.8% according to ReaxFF and DFT, respectively, with respect to the stoichiometric structure.

3.2. Stoichiometric and Reduced CeO_2 Surfaces.

Among the possible ceria surfaces, only the principal (111) surface termination was considered in the fitting, while the other low index surfaces, CeO_2 (110) and the reconstructed CeO_2 (100), were considered for the validation of the potential. In addition to the stoichiometric CeO_2 (111), two defective structures were included, with the oxygen vacancy located in the first and the third O layers (see Figure 4).

A supercell 2×2 of the unit cell was used to model the surface (111), formed by 9 atomic layers and with stoichiometry $\text{Ce}_{12}\text{O}_{24}$. One of the 4 oxygen atoms in each the topmost and the third layer was removed to model the surface/subsurface oxygen vacancy, resulting in a defect concentration θ of 1/4 in the surface layer. The ReaxFF calculations predict the subsurface vacancy more stable by 0.14 eV, in reasonable agreement with the PBE0 calculations of 0.23 eV.⁸⁰ The formation energies are reported in Table 5.

The surface reactivity may be affected by this observation since these defects could be segregated in the subsurface layer, thus preventing the filling of the vacancy by the species interacting with the surfaces, as H_2O and O_2 .^{80–82}

To validate further the new parameterization, we computed the surface energies (E_s) of the three low index surfaces (111), (110), and (100). The same supercells adopted by Broqvist *et al.*⁴⁴ were used here: a 4×4 unit cell with 14, 20, and 8 CeO_2 atomic layers for the (111) surface, the (110) surface, and the reconstructed (100) surface, respectively. The surface (100) was reconstructed by moving half of the O rows from one termination to the other to quench the dipole moment of the surface.

Surface energies (E_s) were calculated according to the equation

$$E_s = \frac{E_{\text{slab}} - NE_{\text{bulk}}}{2A} \quad (8)$$

where E_{slab} , E_{bulk} , N , and A are the energy of the surface model and the crystallographic unit cell of CeO_2 , the number of formula units of CeO_2 forming the slab, and the surface area of the slab, respectively.

In the PBE0 and ReaxFF calculations, the cell parameters of the slab models were fixed at the optimal bulk value computed with the corresponding method, while no constraints were applied on the atomic positions. The results are listed in Table 6. The PBE0 results are in good agreement with the previous calculations performed with different DFT methods.²⁰ The relative stabilities of the three surfaces are correctly described by the ReaxFF, even though the E_s of the (100) surface was overestimated compared to both the DFT and the original potential values.

Subsequently, the oxygen vacancies at the surfaces (110) and (100) were examined. Two supercells p(2×1) and c(2×2) were adopted for the (110) and (100) surfaces, respectively, to have a surface defect concentration θ of 1/4 as for the (111) surface. The slabs contain 7 and 13 atomic layers for the (110) and (100) surface models, respectively. As for the previous case, the PBE0/ReaxFF optimized cell parameters for the bulk were assumed and fixed in the surface relaxation, while all the atom coordinates were fully relaxed. The results are reported in

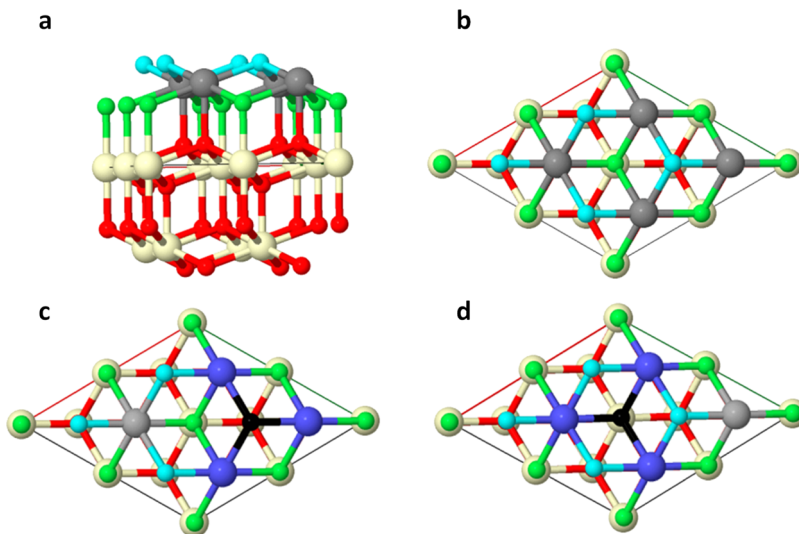


Figure 4. Side (a) and top (b) view of the CeO_2 111 $p(2 \times 2)$ slab and model of an oxygen vacancy on the topmost O layer (c) and in the subsurface O layer (d). In (a) and (b), the surface O layer is represented in light blue, the subsurface O layer is represented in light green. Between the two, the Ce layer is represented in gray. The underneath layers of O and Ce are represented in red and white, respectively. In (c) and (d), three Ce atoms in the first cationic shell of the vacancy (nearest neighbors, nns) are represented in cyan. Ce atoms in the second cationic sphere of the vacancy (next nearest neighbor, nnn) are represented in gray.

Table 5. Energy of Formation of the O Vacancy E_{fv} (eV) in the Surface (1L) and Subsurface (3L) O Layer of the Surface 111 $p(2 \times 2)$ Model

method	E_{fv}		
	1L	3L	ΔE_{fv}
ReaxFF (this work)	3.18	3.04	-0.14
ReaxFF ^{44a}	3.32	3.63	0.31
PBE0 (this work)	3.00	2.77	-0.23

^aOriginal Ce–O ReaxFF was reported to reproduce surface defect stability.

Table 6. Computed Surface Energies E_s in J/m²^a

method	111	110	100
PBE0 (this work)	0.86	1.27	1.64
ReaxFF (this work)	0.82	1.09	2.00
ReaxFF ⁴⁴	0.84	1.08	1.63

^aA supercell (2×2) has been used for the surfaces 111, 110, and 100, constituted respectively by 24, 8, and 24 atomic layers and with the same $\text{Ce}_{32}\text{O}_{64}$ stoichiometry. The surface 100 has been reconstructed by moving half the O at the surface termination on top of the opposite Ce termination.

Table 7. The E_{fv} obtained for the models terminated at (110) and (100) are in good agreement with those computed at the DFT level. The lower E_{fv} obtained with our potential for the surface (100) with respect to the PBE0 result is consistent with the higher surface energy predicted by our potential, as reported above.

Table 7. Formation Energies of the Oxygen Vacancy E_{fv} ($1/\text{O}_2$) on Bulk and Low Index Surfaces of CeO_2 , in eV

method	bulk	(111)	(110)	(100)
ReaxFF (this work)	4.16	3.18/3.04	2.71	1.98
ReaxFF ⁴⁴	4.80	3.32/3.63	3.15	2.35
PBE0 (this work)	3.84	3.00/2.77	2.64	2.33

It is worth noting that only the structures of the defects in the bulk and on the (111) surface and the relative stabilities of the surface/subsurface vacancies were used for the training dataset, while the energies included in the fitting are only the experimental cohesive energies of γ -Ce, CeO_2 , and Ce_2O_3 . Therefore, our new parameter set is able to reproduce the relative stabilities of the ceria surfaces and energy of formation of vacancies in the bulk and on the surfaces.

3.3. H₂ and H₂O on CeO₂(111). It is worth to highlight that the parameters for the bonding, bending, and a van der Waals terms for the species Ce/H and Ce/O/H were not available. Thus, this is the first work that attempted the parameterization of the potential terms involving these species. Here, the van der Waals term for Ce/H was parameterized to reproduce the PES when an H₂ molecule approaches to CeO₂ (111) surface, as shown in Figure 5. The slab model of the surface (111) adopted to examine oxygen vacancies was used throughout these adsorption studies.

The ReaxFF accurately reproduced the PES curvature near the minimum, located at 3.35 Å, but the potential curve is less steep compared to the DFT. In addition, the ReaxFF energy increases until the H₂ molecule separates from the surface to the cutoff distance of 10 Å, which demonstrates the long-range interaction. The continuous increase of the interaction energy with the distance is not ascribed to the van der Waals potential but attributed to an erroneous charge partition by the EEM method, as already reported by Broqvist *et al.*⁴⁴ for the interaction CeO₂/O₂. This is because the EEM method sets a small unphysical positive charge on hydrogen of H₂ (0.064 | e⁻|) and thus slightly negatively charge to the CeO₂ surface, resulting in an incorrect Coulomb interaction in the long-range limit. To quantify the effects of this error on the interaction of H₂–CeO₂(111), the adsorption energies were computed with two distinct methods, the in-cell and out-cell ones. With the out-cell method, the E_{ads} (out-cell) is computed according to E_{ads} (out-cell) = E (H₂/surface) – E (H₂) – E (slab) = -0.16 eV, where E (H₂/surface), E (H₂), and E (slab) are respectively the energies of the adsorbed system, the isolated

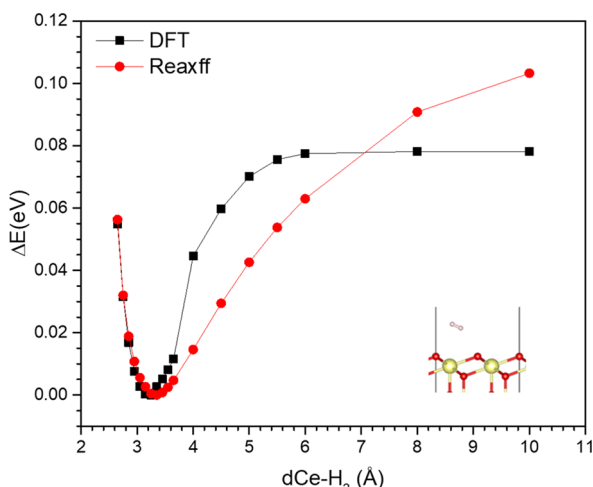


Figure 5. PES for the Ce–H₂ distance on CeO₂(111), considering a trajectory of the molecule orthogonal to the surface. The distance is calculated between the barycenter of H₂ and the nearest Ce ion.

H₂, and isolated surface computed with distinct simulation boxes. With the in-cell method, E_{ads} (in-cell) = E_{ads} (in-cell) = $E(\text{H}_2/\text{surface}) - E(\text{H}_2 + \text{slab}) = -0.11$ eV. Here, $E(\text{H}_2 + \text{slab})$ is the energy of the isolated H₂ and surfaces inside the same cell, which is affected by the error in charge distribution and makes the adsorption energy more endothermic of 0.05 eV, which is closer to the PBE0 value of 0.07 eV.

Then, the parameterizations of the bonding and angle terms were performed by including the PESs corresponding to the dissociation of H₂ and H₂O on CeO₂(111) in the training dataset, as shown in Figure 6 and Figure 7a, respectively. The PES for the H₂ dissociation is remarkably well reproduced by

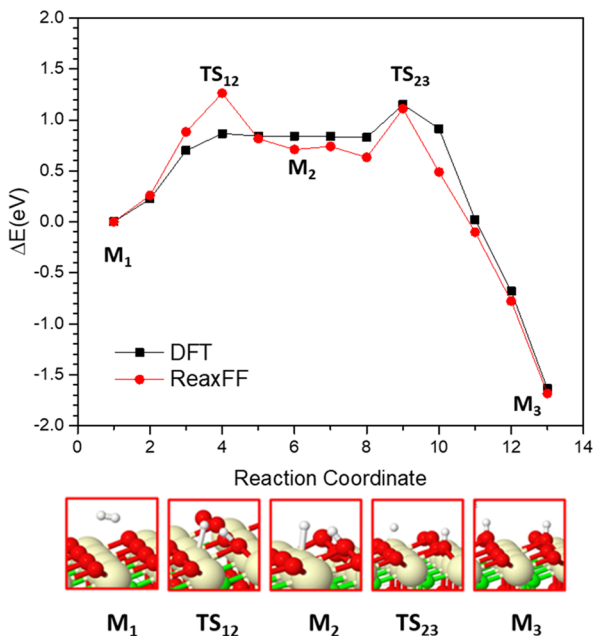


Figure 6. MEP corresponding to the dissociation of the H₂ adsorbed on CeO₂(111). The minima structures M₁, M₂, and M₃ are respectively to the adsorbed H₂, the heterolytic dissociation product, and the homolytic dissociation product. The transition states structures TS₁₂ and TS₂₃ connecting the corresponding minima have been included.

the ReaxFF, whereas the energy barrier for dissociation of water was slightly overestimated.

Finally, the potential was refined on the minima structures corresponding to the water adsorbed in the associated forms (H₂O) and dissociated forms (HO-H) on CeO₂(111). For the associated form, two quasi-degenerate conformers exist.³⁴ They differ for the water forming one or two H-bond with the surface oxygen atoms, here called H₂O-h1 and H₂O-h2, respectively. According to the PBE0 calculations, the H₂O-h2 is more stable by only 0.03 eV and it was the only one considered in the parameter fitting. Figure 8 depicts the associated and dissociated water molecules on CeO₂(111) adopted in the parameter fitting. The adsorption energies, the cerium–water distances, and the main H-bonds obtained by the optimized ReaxFF parameter set are compared with DFT data for the (111) surface in Table 8, Table 9, and Table 10, respectively. In these tables, the properties for the (110) and (100) surfaces are also summarized as a result of the validation test to confirm the applicability of the optimized parameter set to the other surfaces, as discussed later.

The DFT results show that the stability of the system with the dissociated water is almost isoenergetic with the associated one. Our ReaxFF results reproduce the DFT data fairly well even for the (111) surface on which water is dissociatively adsorbed with a more stabilized structure. The ReaxFF model forms shorter H-bonds between the water and the ceria surfaces (see Table 10), which causes the irregular PES (red curve of Figure 7a) in the first segment of the dissociation when the structures obtained by DFT were assumed. After the fitting, the MEP was recalculated by adopting the nudged elastic method (NEB),⁸³ which provides a smoother PES (blue curve in Figure 7a) with an activation energy of 0.20 eV, which agrees well with the PBE0 value of 0.15 eV. For the inverse process, the barriers are 0.34 and 0.11 eV according to the ReaxFF and PBE0, respectively.

Figure 7b reports the PES relative to the water adsorption on the CeO₂(111) surface. It is worth highlighting that, although this was not used in the training set, the ReaxFF data are in excellent agreement with DFT data.

3.4. H₂O on CeO₂(110) and CeO₂(100): Static Calculations. The Ce/O/H potential parameters fitted using the CeO₂(111) data were validated against the water adsorption on the other low index surfaces, CeO₂(110) and CeO₂(100), as depicted respectively in Figure 9 and Figure 10. The geometrical aspects of the surface (110) are well reproduced, apart from the underestimated H-bond length commonly recognized in the other cases. The energetics of adsorption and dissociation are barely more exothermic than on the surface (111) and underestimated compared to the PBE0 results. The ReaxFF shows that water dissociates on the (100) surface with an exothermic reaction of 2.00/2.20 eV, which agrees with DFT, while the molecularly adsorbed state was not isolated by the ReaxFF. This is due to a negligible kinetic barrier associated with the dissociation process, as found by other theoretical calculations.¹⁹

The magnitude of the absorption energies discussed above for the (111) and (100) surfaces are in agreement with experimental investigations at cryogenic temperature and at low pressure, which have shown that the CeO₂(100) surface exposed to water vapor is more reactive than the (111) surface, forming the double hydroxyls.¹⁰ Moreover, all the water seems to desorb from CeO₂(111) at temperatures ranging between

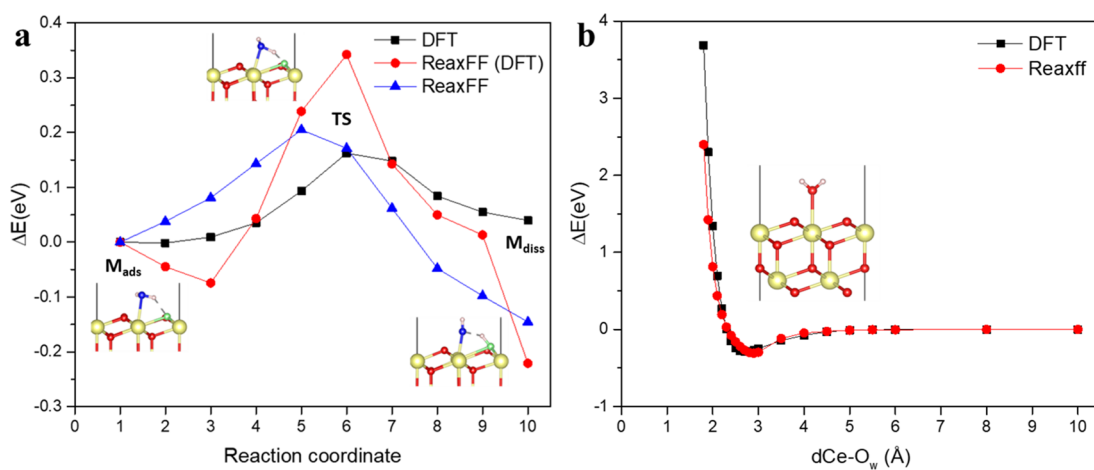


Figure 7. (a) MEP corresponding to the dissociation of the H_2O adsorbed on CeO_2 (111). Captions depicted the DFT structures of the adsorbed water (M_{ads}), the transition state (TS), and the dissociated water (M_{diss}). (b) PES of water adsorption on CeO_2 (111).

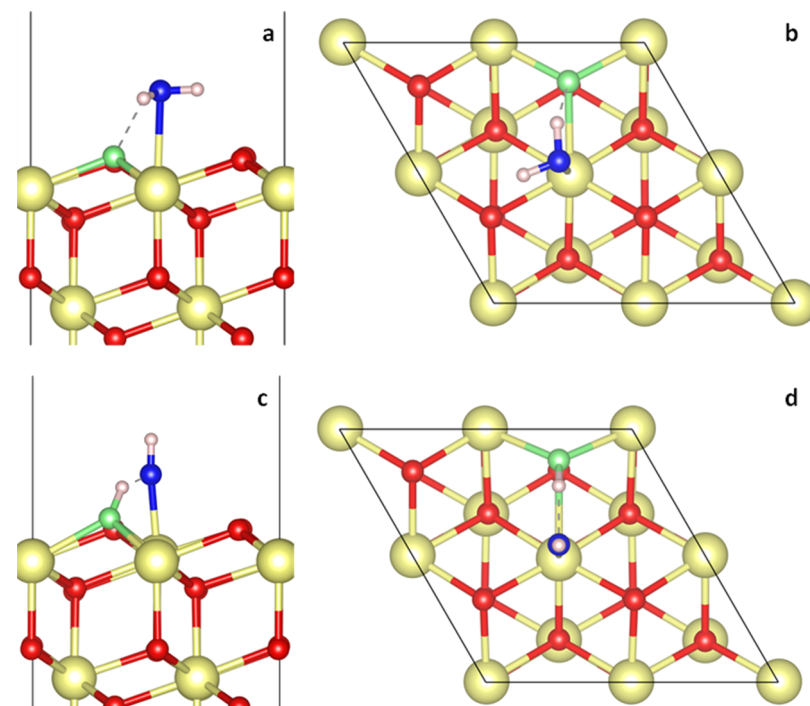


Figure 8. Side view and top view of H_2O adsorbed (a, b) and dissociated (c, d) on CeO_2 (111). The O of water is colored in blue, the surface O receiving the H in light green.

Table 8. Water Adsorption Energies (E_{ads}) on CeO_2 (111) in the Associated (H_2O) and Dissociated ($\text{HO}-\text{H}$) Forms, in eV

method	111		110		100	
	H_2O	$\text{HO}-\text{H}$	H_2O	$\text{HO}-\text{H}$	H_2O	$\text{HO}-\text{H}$
ReaxFF	-0.50 ^a /-0.48 ^b	-0.64	-0.58	-0.68		-2.00 ^c /-2.20 ^d
PBE0	-0.53 ^a /-0.51 ^b	-0.50	-1.44	-1.76	-1.65	-2.24 ^c

^aConformer h2. ^bConformer h1. ^cConformer for $\text{H}-\text{OH}$ corresponding to the PBE0 structures. ^dConformer with a different H-bond network.

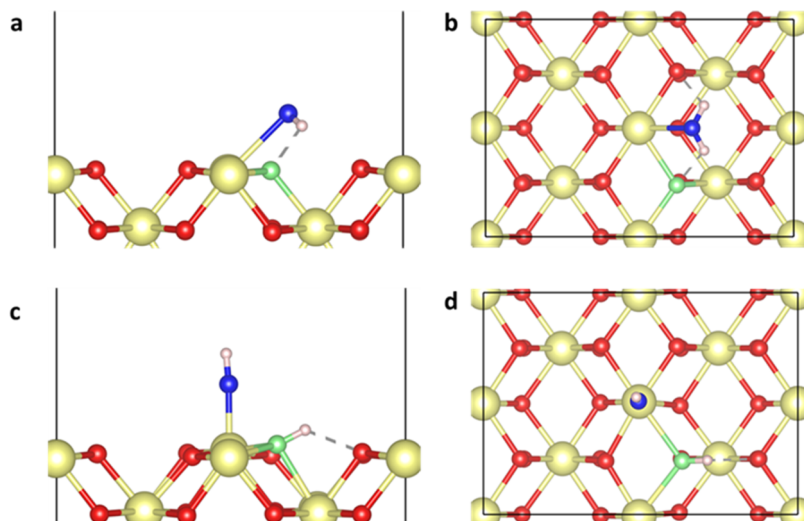
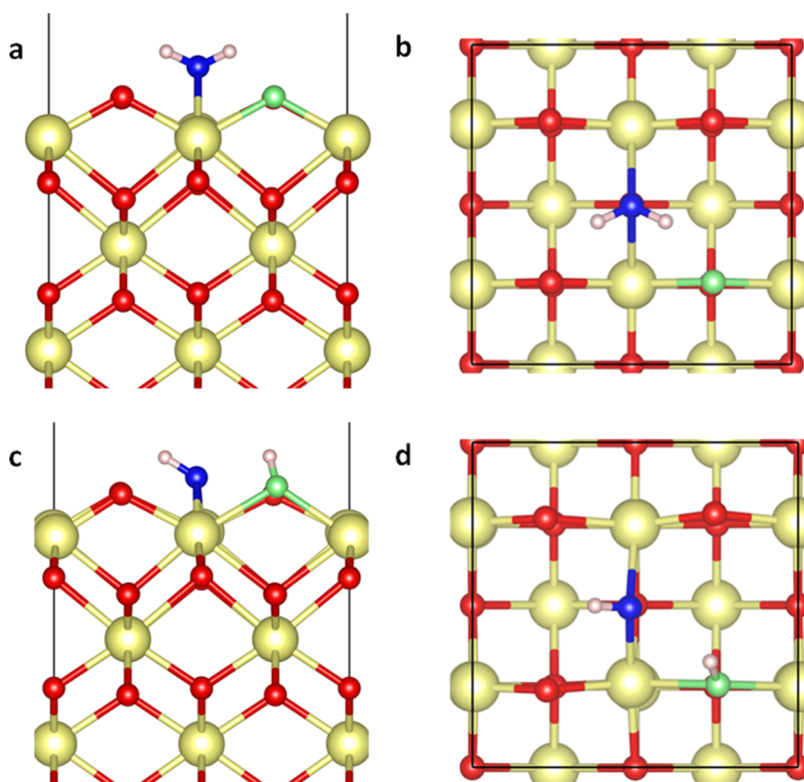
Table 9. Bond Lengths between the Adsorbed O of Water (O_w) and Underneath Ce, in Å

method	111		110		100	
	H_2O	$\text{HO}-\text{H}$	H_2O	$\text{HO}-\text{H}$	H_2O	$\text{HO}-\text{H}$
ReaxFF	2.708 ^a /2.708 ^b	2.169	2.654	2.113		2.287–2.402 ^c /2.336–2.371 ^d
PBE0	2.578 ^a /2.616 ^b	2.225	2.631	2.090	2.600/2.626	2.293–2.401 ^d

^aConformer h2. ^bConformer h1. ^cConformer for $\text{H}-\text{OH}$ corresponding to the PBE0 structures. ^dConformer with a different H-bond network.

Table 10. Main Lengths of the Hydrogen Bonds between the Water and the Ceria Surfaces, in Å

method	111		110		100	
	H ₂ O	HO-H	H ₂ O	HO-H	H ₂ O	HO-H
ReaxFF	1.617–1.617/1.582	1.581	1.654/1.654	1.581	2.161/2.170	2.060/1.578
PBE0	1.813–2.132/-	1.575	2.079/2.080	1.900	2.346/-	

**Figure 9.** Side view and top view of the PBE0 optimized structures of H_2O adsorbed (a, b) and dissociated (c, d) on CeO_2 (110). The O of water is colored in blue, the surface O receiving the H in light green.**Figure 10.** Side view and top view of the PBE0 optimized structures of H_2O adsorbed (a, b) and dissociated (c, d) on CeO_2 (100). The O of the water is colored in blue, the surface O receiving the H in light green.

200 and 300 K, whereas on CeO_2 (100), the last hydroxyl groups reacts to form water molecules at above 500 K.

3.5. MD Simulations of Water Adsorption and Dissociation at Ceria (111) and (100) Surfaces.

CeO_2 (111). To simulate liquid water on CeO_2 (111), the slab and a

box of bulk water were first thermally equilibrated, individually, then the two simulation boxes were united to form a layered CeO_2 (111)/ H_2O model with periodic boundary condition even along the z direction. The simulations were run for over 800 ps. A representative snapshot of the equilibrated structure

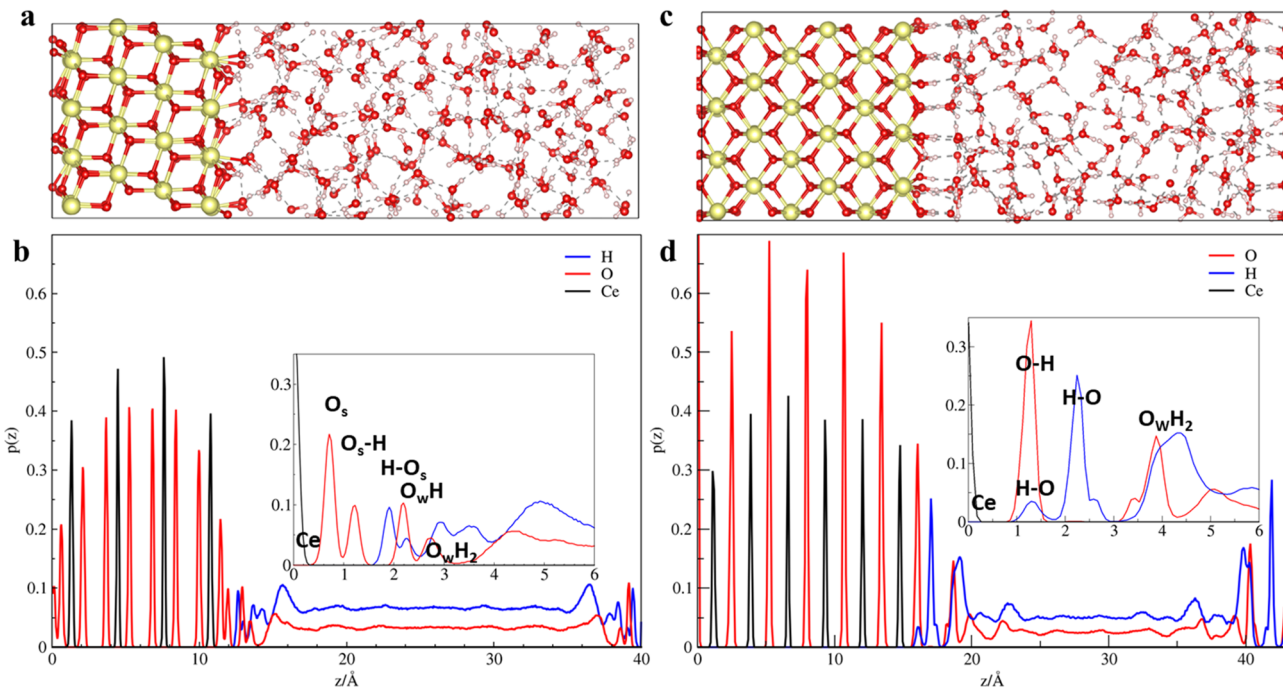


Figure 11. (a) Equilibrated snapshot of the $\text{CeO}_2(111)$ –water model; (b) density plot of the H, O, and Ce species along the z axis of model (a). (c) Equilibrated snapshot of the $\text{CeO}_2(100)$ –water model; (d) density plot of the H, O, Ce species along the z axis of model (c). Insets in (b) and (d) are the corresponding plot magnification of the interphase zone, with the x -axis origin settled on the outermost right Ce layer.

is shown in Figure 11a. Figure 12 shows the temporal evolutions of the surface coverage θ by the three species (H_2O –Ce: molecularly adsorbed water, HO –Ce: dissociated water, and O_sH : protonated surface oxygens) on the ceria surface. Water is considered adsorbed when the distance between O and Ce is within 3 Å.

The (111) surface model is composed of active sites at the topmost surface O (O_s), an acceptor of H from water, and Ce, an acceptor of either H_2O or OH. On the clean surface, they are in equal number: in the considered model, there are 16 Ce and 16 O_s for both slab terminations. Water dissociation occurred from the very beginning of the MD simulations, resulting a steep decrease in the adsorbed water (H_2O –Ce, θ from 0.6 to 0.15) and increase in the surface hydroxyls (HO –Ce and O_sH , θ to 0.35) (Figure 12a). The equilibration was reached after 100 ps when about 35% of cerium sites were hydroxylated. It is interesting to observe that, during hydroxylation of the surface, the molecularly adsorbed water decreases because a part of water dissociates and the rest desorbs, as observed in previous DFT simulations.³¹ This is also observed as the increase in free Ce ions on the surface (black curve in Figure 12a).

The analysis of the distribution probability of each species along the z axis in Figure 11b allows us to understand how the species are bound on the (111) surface. The oxygen (O_s) at the topmost surface is 0.73 Å away from the underneath Ce layer, while the protonated oxygen (O_sH) is displaced to 1.25 Å from the Ce layer. The closest species to the surface oxygen is the H from the protonated sites (at around 1.9 Å) followed by the hydroxyl group from the dissociated water (2.25 Å) adsorbed on the Ce site. The oxygen peaks at 2.73 Å and 4.50 Å are assigned to water molecules interacting with the surface as the first and second shell of adsorbed water. The water molecules locating far from the surface are expected to behave like bulk liquid. According to the results, water, both in

hydroxylated and molecular forms, covered only the 55% of the available Ce sites, and does not form a full monolayer as shown in Figure 13a.

This is explained with higher stabilization of the water–water with respect to the water–surface interactions, as suggest by static DFT calculations.³¹

CeO_2 (100). The same computational setting adopted to model the water/ CeO_2 (111) was also used for CeO_2 (100). A representative snapshot of the equilibrated structure is shown in Figure 11c. The topmost layer is composed of 16 active O sites as proton acceptors; 16 Ce in the underneath layer can bind both water and OH^- , as in the case of the (111) surface. Because the Ce in (100) surface coordinates fewer oxygens (6-O) with respect to the (111) surface (7-O), each Ce can bind up to 2 OH^- or H_2O species.

Figure 12b shows that the adsorbed water molecules dissociated completely within the first ps of the simulation: then the other water molecules dissociated without prior adsorption on the Ce sites following the mechanism described in the next section, that is, the adsorbed water species immediately disappears. After only 120 ps, the system seems to reach equilibration with an average hydroxyl coverage of 0.91, in excellent agreement with the recent fast H-MAS NMR experiments that revealed a coverage of about 0.9.¹⁹ Figure 13 shows that each adsorbed OH^- locates at a bridging site between two Ce as in the case of the DFT simulations, which evaluated adsorption geometry of OH^- at the gas phase (see Figure 10c,d).

The probability distribution of the species along the z axis reported in Figure 11d exhibits a single peak for the oxygen, which locates at 1.25 Å above the Ce layer, contrary to the (111) surface that possesses two peaks in the vicinity of the surface: here the (100) surface is mostly hydroxylated, and the hydroxyl moieties form a strong H-bond between vicinal O_sH and O_s sites, as indicated by the clear overlap between the

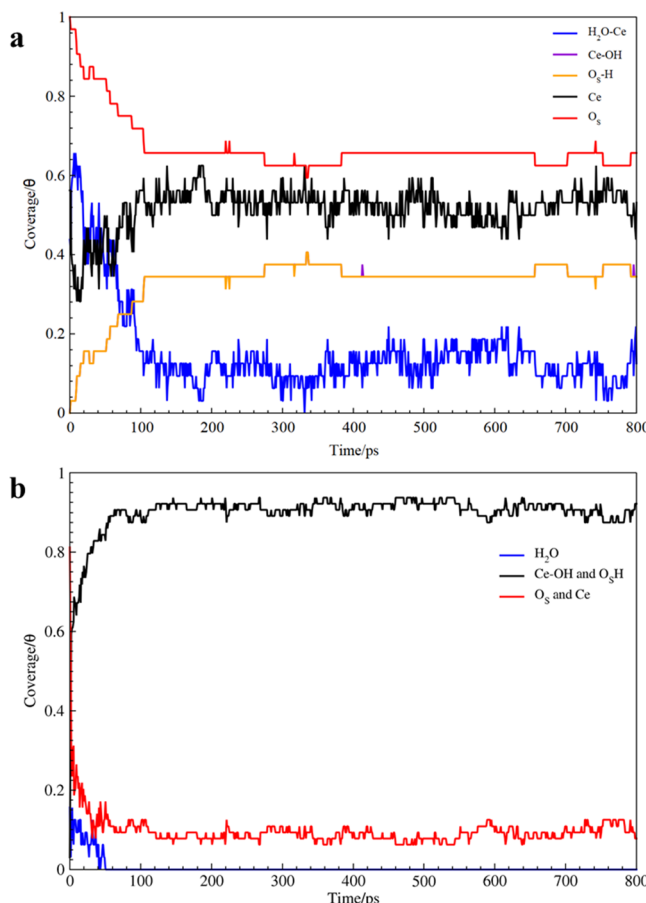


Figure 12. Time evolution of the different species coverage on the (a) CeO₂ (111) and (b) CeO₂ (100) surface terminations. The labels indicated the free surface sites of Ce and O (O_s), the water molecularly adsorbed (H₂O-Ce), the OH⁻ from the dissociated water adsorbed (HO-Ce), and the protonated surface O (O_sH).

first H peak and the first O peak, among which the proton transfer is possible. The second H peak that is located away from the O–H peaks by approximately 0.97 Å is attributed to the H of the hydroxyl directing toward the O of neighbor water, whose corresponding peak appears at 1.60 Å apart. At the region far from the surface, the probability distributions of oxygen and hydrogen resemble those of bulk water.

3.5.1. Surface Coverage and H-Bond Network on the (111) and (100) Surfaces.

As shown in Figure 13, the H-bond network formed at the ceria–water interface differs greatly for the two surfaces.

On CeO₂ (111), most of the hydroxyl groups are separated from each other, i.e., they are not bridged between two Ce cations. At the same time, water adsorption seems to occur more frequently on the free Ce ions at the surface not involved with hydroxyls. On the hydroxyl pairs found at the surface, the O_sH group always acts as H donor to the Ce–OH group (bond length 1.57–1.68 Å), whereas the latter can form H-bonds with water in the liquid phase.

On CeO₂ (100), the surface hydroxyls form either H-bond with the other O along the surface plane and with water in the liquid phase. As shown by the density of the species plot (see Figure 11d), the H-bonds between hydroxyl groups and water are much more frequent, with an average bond length of 1.80 Å. On the surface plane, the average H-bond length is 1.82 Å, with extremes of 1.54–2.22 Å.

On the interphase hydroxylated interfaces, it is observed a more extended H-bond network on CeO₂(100): most of the water molecules received an H-bond by the surface OH and form 1 or 2 other H-bonds with the molecules on the same plane, with an average length of 1.76 Å. On CeO₂ (111), the H-bond network is less extended and with a longer average length of 1.90 Å. This difference is due to the lower hydroxyl's coverage of the (111) surface in comparison with the (100), the longer distances between surface oxygens on the (111) surface with respect to the (100),³¹ and the lower number of H-bridges that the (111) surface can establish with liquid water.

3.5.2. Mechanisms of Water Dissociation on the Two Surfaces.

Figure 14 shows the mechanisms of water dissociation observed on the two surfaces investigated. For the (111) surface, the mechanism is independent on the degree of hydroxylation, whereas for the (100) surface, two mechanisms are observed for the clean and hydroxylated surfaces, respectively.

On the surface (111), water must first absorb on a Ce site, form H-bridge with a nearby Os and from here proton transfer is then possible (Figure 14a–c).

On the dry CeO₂ (100) surface, water dissociation occurs at the very beginning of the simulation following the mechanism as depicted in the Figure 14: water adsorbs above between two

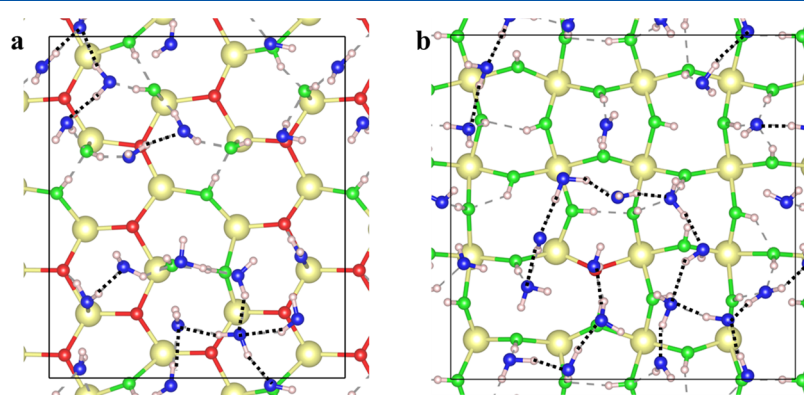


Figure 13. Models of (a) CeO₂ (111) and (b) CeO₂ (100) surfaces with adsorbed/dissociated water molecules extracted from the interface ceria/liquid water investigated in the previous paragraph. Oxygen atoms of water, hydroxyl, and surface sites are colored respectively in blue, green, and red. Gray dashed lines suggest the H-bond network between water and hydroxyl.

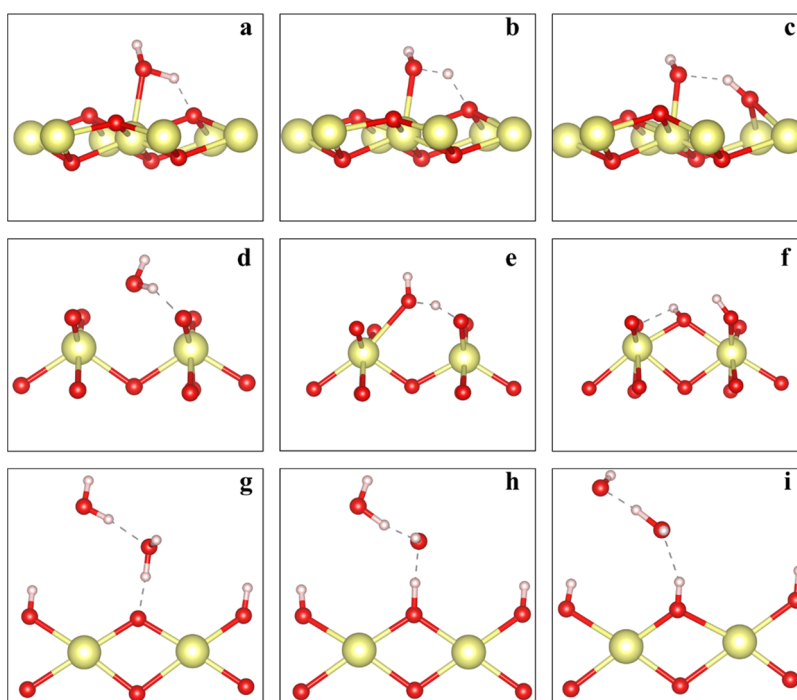


Figure 14. Mechanisms of water dissociation and surface hydroxylation of (a–c) CeO_2 (111) dry, (d–f) CeO_2 (100) dry, and (g–i) CeO_2 (100) 90% hydroxylated.

unsaturated Ce ions forming an H-bond with one of the surface O (Figure 14d), then water is driven by one of the cations while the proton transfer occurs (Figure 14e).

Subsequently, on the hydroxylated surface, a dynamic proton exchange is observed between the surface and the liquid phase (see Figure 14g–i): water protonates the O sites without Ce mediation, while the OH^- formed can deprotonate either a nearby water molecule or surface hydroxyl. As shown by the coverage profiles (Figure 11a,b), the amount of surface hydroxyls on (100) fluctuates greatly over the course of the dynamics, suggesting greater reactivity than on the surface (111), where water dissociation and recombination are much slower.

4. CONCLUSIONS

In this work, a reactive force field was developed for the Ce–O–H systems. First, the available Ce–O ReaxFF parameter set was re-parameterized by adopting a training dataset computed at the DFT/PBE0 level. The theoretical dataset comprises the structures, energies, and mechanical properties of the crystalline phase of the CeO_2 and Ce_2O_3 , besides the (111) surface and O-defective structures of the surface and bulk. The CeO_2 crystalline phase was satisfactorily reproduced, while larger deviations on the structural and mechanical properties of the reduced oxide Ce_2O_3 were found. Nevertheless, the formation energies of the oxygen vacancies and some structural features of the defective structures are well reproduced. The localization of negative charge estimated by DFT at the reduced Ce^{3+} site in the O defect model cannot be reproduced by ReaxFF, which instead distributes the negative charge equally on the 4 Ce surrounding the vacancy. This is an inherent limitation of the EEM scheme employed, which is not able to reproduce the integer charge discontinuity occurring in a QM treatment. However, this should not invalidate the new

parameter set to describe processes not involving electronic transfers between ceria and substrates.

A further parameterization of the ReaxFF to include the interaction with hydrogen was carried out using additional training dataset composed of the structures and energies of H_2 and H_2O adsorbed and dissociated on the CeO_2 (111) surface. The potential energy surfaces for the considered processes were reproduced fairly well. For the water molecule on the (111) surface, the dissociated state is stabilized by 0.14 eV compared to the molecular state, while according to DFT calculations, the two states are almost equally stable. The potential energy profiles evaluated by DFT for the water adsorption on the ceria (110) and (100) surfaces were accurately reproduced.

MD simulations with the new parameter set were performed to simulate the ceria/liquid water interface with (111) and (100) surfaces at 300 K. Approximately 35% of the surface sites of CeO_2 (111) are hydroxylated and adsorbed water covers about the 15% of the surface, while 90% of the CeO_2 (100) surface is hydroxylated and no water molecule is adsorbed. From these data, the computed average hydroxyl concentration is 5.6 nm^{-2} on the surface (111), whereas on the (100) surface, it is 12.3 nm^{-2} . The higher OH coverage of the surface 100 results in a more extended network of H-bridges with water molecules at the interface.

The good agreement with DFT calculations and experimental findings suggest that this new potential is a promising candidate for further studies of molecular dynamics of the reactivity of the ceria surfaces in water.

■ ASSOCIATED CONTENT

● Supporting Information

The Supporting Information is available free of charge at <https://pubs.acs.org/doi/10.1021/acs.jpca.1c04078>.

The GULP library file containing all the ReaxFF parameters used in this work to study ceria/water interfaces ([PDF](#))

AUTHOR INFORMATION

Corresponding Author

Alfonso Pedone – Department of Chemical and Geological Sciences, University of Modena and Reggio Emilia, Modena 41125, Italy;  [orcid.org/0000-0003-3772-7222](#); Email: alfonso.pedone@unimore.it

Authors

Luca Brugnoli – Department of Chemical and Geological Sciences, University of Modena and Reggio Emilia, Modena 41125, Italy

Maria Cristina Menziani – Department of Chemical and Geological Sciences, University of Modena and Reggio Emilia, Modena 41125, Italy;  [orcid.org/0000-0003-3428-5297](#)

Shingo Urata – Innovative Technology Laboratories, AGC Inc., Yokohama, Kanagawa 230-0045, Japan;  [orcid.org/0000-0001-6878-345X](#)

Complete contact information is available at:

<https://pubs.acs.org/10.1021/acs.jpca.1c04078>

Author Contributions

L.B. performed all the simulations and co-wrote the manuscript. M.C.M. read and revised the manuscript. S.U. co-wrote the manuscript. A.P. designed the work and co-wrote the manuscript.

Notes

The authors declare no competing financial interest.

ACKNOWLEDGMENTS

This work was supported by AGC Inc. through a research contract signed with A.P.

REFERENCES

- (1) Montini, T.; Melchionna, M.; Monai, M.; Fornasiero, P. Fundamentals and Catalytic Applications of CeO₂-Based Materials. *Chem. Rev.* **2016**, *116*, 5987–6041.
- (2) Aneggi, E.; Boaro, M.; Colussi, S.; de Leitenburg, C.; Trovarelli, A. Chapter 289 - Ceria-Based Materials in Catalysis: Historical Perspective and Future Trends. In *Handbook on the Physics and Chemistry of Rare Earths*; Bünnli, J.-C. G., Pecharsky, V. K., Eds.; Including Actinides; Elsevier, 2016; Vol. 50, pp. 209–242, DOI: [10.1016/bs.hpcr.2016.05.002](https://doi.org/10.1016/bs.hpcr.2016.05.002).
- (3) Hedrick, J. B.; Sinha, S. P. Cerium-Based Polishing Compounds: Discovery to Manufacture. *J. Alloys Compd.* **1994**, *207-208*, 377–382.
- (4) Bouzid, D.; Belkhie, N.; Aliouane, T. Optical Glass Surfaces Polishing by Cerium Oxide Particles. *IOP Conf. Ser.: Mater. Sci. Eng.* **2012**, *28*, 012007.
- (5) Pharmacological potential of cerium oxide nanoparticles - Nanoscale (RSC Publishing) <https://pubs.rsc.org/az/content/articlelanding/2011/nr/c0nr00875c/unauth#divAbstract> (accessed 2021-03-07).
- (6) Caputo, F.; Mameli, M.; Sienkiewicz, A.; Licoccia, S.; Stellacci, F.; Ghibelli, L.; Traversa, E. A Novel Synthetic Approach of Cerium Oxide Nanoparticles with Improved Biomedical Activity. *Sci. Rep.* **2017**, *7*, 4636.
- (7) Das, S.; Dowding, J. M.; Klump, K. E.; McGinnis, J. F.; Self, W.; Seal, S. Cerium Oxide Nanoparticles: Applications and Prospects in Nanomedicine. *Nanomedicine* **2013**, *8*, 1483–1508.
- (8) Mullins, D. R. The Surface Chemistry of Cerium Oxide. *Surf. Sci. Rep.* **2015**, *70*, 42–85.
- (9) Henderson, M. A.; Perkins, C. L.; Engelhard, M. H.; Thevuthasan, S.; Peden, C. H. F. Redox Properties of Water on the Oxidized and Reduced Surfaces of CeO₂. *Surf. Sci.* **2003**, *S26*, 1–18.
- (10) Mullins, D. R.; Albrecht, P. M.; Chen, T.-L.; Calaza, F. C.; Biegalski, M. D.; Christen, H. M.; Overbury, S. H. Water Dissociation on CeO₂(100) and CeO₂(111) Thin Films. *J. Phys. Chem. C* **2012**, *116*, 19419–19428.
- (11) Gritschneider, S.; Reichling, M. Structural Elements of CeO₂(111) Surfaces. *Nanotechnology* **2007**, *18*, No. 044024.
- (12) Chen, B.; Ma, Y.; Ding, L.; Xu, L.; Wu, Z.; Yuan, Q.; Huang, W. Reactivity of Hydroxyls and Water on a CeO₂(111) Thin Film Surface: The Role of Oxygen Vacancy. *J. Phys. Chem. C* **2013**, *117*, 5800–5810.
- (13) Torbrügge, S.; Custance, O.; Morita, S.; Reichling, M. Manipulation of Individual Water Molecules on CeO₂(111). *J. Phys.: Condens. Matter* **2012**, *24*, No. 084010.
- (14) Matolín, V.; Matolínová, I.; Dvořák, F.; Johánek, V.; Mysliveček, J.; Prince, K. C.; Skála, T.; Stetsovych, O.; Tsud, N.; Václavů, M.; Šmid, B. Water Interaction with CeO₂(111)/Cu(111) Model Catalyst Surface. *Catal. Today* **2012**, *181*, 124–132.
- (15) Kundakovic, L.; Mullins, D. R.; Overbury, S. H. Adsorption and Reaction of H₂O and CO on Oxidized and Reduced Rh/CeO_x(111) Surfaces. *Surf. Sci.* **2000**, *457*, 51–62.
- (16) Herman, G. S.; Kim, Y. J.; Chambers, S. A.; Peden, C. H. F. Interaction of D₂O with CeO₂(001) Investigated by Temperature-Programmed Desorption and X-Ray Photoelectron Spectroscopy. *Langmuir* **1999**, *15*, 3993–3997.
- (17) Lykhach, Y.; Johánek, V.; Aleksandrov, H. A.; Kozlov, S. M.; Happel, M.; Skála, T.; Petkov, P. S.; Tsud, N.; Vayssilov, G. N.; Prince, K. C.; Neyman, K. M.; Matolín, V.; Libuda, J. Water Chemistry on Model Ceria and Pt/Ceria Catalysts. *J. Phys. Chem. C* **2012**, *116*, 12103–12113.
- (18) Senanayake, S. D.; Stacchiola, D.; Evans, J.; Estrella, M.; Barrio, L.; Pérez, M.; Hrbek, J.; Rodriguez, J. A. Probing the Reaction Intermediates for the Water–Gas Shift over Inverse CeO_x/Au(111) Catalysts. *J. Catal.* **2010**, *271*, 392–400.
- (19) Gill, L.; Beste, A.; Chen, B.; Li, M.; Mann, A. K. P.; Overbury, S. H.; Hagaman, E. W. Fast MAS 1H NMR Study of Water Adsorption and Dissociation on the (100) Surface of Ceria Nanocubes: A Fully Hydroxylated, Hydrophobic Ceria Surface. *J. Phys. Chem. C* **2017**, *121*, 7450–7465.
- (20) Paier, J.; Penschke, C.; Sauer, J. Oxygen Defects and Surface Chemistry of Ceria: Quantum Chemical Studies Compared to Experiment. *Chem. Rev.* **2013**, *113*, 3949–3985.
- (21) Kumar, S.; Schelling, P. K. Density Functional Theory Study of Water Adsorption at Reduced and Stoichiometric Ceria (111) Surfaces. *J. Chem. Phys.* **2006**, *125*, 204704.
- (22) Fronzi, M.; Assadi, M. H. N.; Hanaor, D. A. H. Theoretical Insights into the Hydrophobicity of Low Index CeO₂ Surfaces. *Appl. Surf. Sci.* **2019**, *478*, 68–74.
- (23) Chen, H.-T.; Choi, Y. M.; Liu, M.; Lin, M. C. A Theoretical Study of Surface Reduction Mechanisms of CeO₂(111) and (110) by H₂. *ChemPhysChem* **2007**, *8*, 849–855.
- (24) Watkins, M. B.; Foster, A. S.; Shluger, A. L. Hydrogen Cycle on CeO₂ (111) Surfaces: Density Functional Theory Calculations. *J. Phys. Chem. C* **2007**, *111*, 15337–15341.
- (25) Molinari, M.; Parker, S. C.; Sayle, D. C.; Islam, M. S. Water Adsorption and Its Effect on the Stability of Low Index Stoichiometric and Reduced Surfaces of Ceria. *J. Phys. Chem. C* **2012**, *116*, 7073–7082.
- (26) Fronzi, M.; Piccinin, S.; Delley, B.; Traversa, E.; Stampfl, C. Water Adsorption on the Stoichiometric and Reduced CeO₂(111) Surface: A First-Principles Investigation. *Phys. Chem. Chem. Phys.* **2009**, *11*, 9188.
- (27) Fernández-Torre, D.; Kośmider, K.; Carrasco, J.; Ganduglia-Pirovano, M. V.; Pérez, R. Insight into the Adsorption of Water on the Clean CeO₂ (111) Surface with van Der Waals and Hybrid Density Functionals. *J. Phys. Chem. C* **2012**, *116*, 13584–13593.

- (28) Yang, Z.; Wang, Q.; Wei, S.; Ma, D.; Sun, Q. The Effect of Environment on the Reaction of Water on the Ceria(111) Surface: A DFT+U Study. *J. Phys. Chem. C* **2010**, *114*, 14891–14899.
- (29) Carchini, G.; García-Melchor, M.; Łodziana, Z.; López, N. Understanding and Tuning the Intrinsic Hydrophobicity of Rare-Earth Oxides: A DFT+U Study. *ACS Appl. Mater. Interfaces* **2016**, *8*, 152–160.
- (30) Farnesi Camellone, M.; Negreiros Ribeiro, F.; Szabová, L.; Tateyama, Y.; Fabris, S. Catalytic Proton Dynamics at the Water/Solid Interface of Ceria-Supported Pt Clusters. *J. Am. Chem. Soc.* **2016**, *138*, 11560–11567.
- (31) Kropp, T.; Paier, J.; Sauer, J. Interactions of Water with the (111) and (100) Surfaces of Ceria. *J. Phys. Chem. C* **2017**, *121*, 21571–21578.
- (32) Marrocchelli, D.; Yıldız, B. First-Principles Assessment of H₂S and H₂O Reaction Mechanisms and the Subsequent Hydrogen Absorption on the CeO₂(111) Surface. *J. Phys. Chem. C* **2012**, *116*, 2411–2424.
- (33) Szabová, L.; Tateyama, Y.; Matolín, V.; Fabris, S. Water Adsorption and Dissociation at Metal-Supported Ceria Thin Films: Thickness and Interface-Proximity Effects Studied with DFT+U Calculations. *J. Phys. Chem. C* **2015**, *119*, 2537.
- (34) Röckert, A.; Kullgren, J.; Broqvist, P.; Alwan, S.; Hermansson, K. The Water/Ceria(111) Interface: Computational Overview and New Structures. *J. Chem. Phys.* **2020**, *152*, 104709.
- (35) van Duin, A. C. T.; Dasgupta, S.; Lorant, F.; Goddard, W. A. ReaxFF: A Reactive Force Field for Hydrocarbons. *J. Phys. Chem. A* **2001**, *105*, 9396–9409.
- (36) Chenoweth, K.; van Duin, A. C. T.; Goddard, W. A. ReaxFF Reactive Force Field for Molecular Dynamics Simulations of Hydrocarbon Oxidation. *J. Phys. Chem. A* **2008**, *112*, 1040–1053.
- (37) Huang, L.; Gubbins, K. E.; Li, L.; Lu, X. Water on Titanium Dioxide Surface: A Revisiting by Reactive Molecular Dynamics Simulations. *Langmuir* **2014**, *30*, 14832–14840.
- (38) Hahn, S. H.; Rimsza, J.; Criscenti, L.; Sun, W.; Deng, L.; Du, J.; Liang, T.; Sinnott, S. B.; van Duin, A. C. T. Development of a ReaxFF Reactive Force Field for NaSiOx/Water Systems and Its Application to Sodium and Proton Self-Diffusion. *J. Phys. Chem. C* **2018**, *122*, 19613–19624.
- (39) Raymond, D.; van Duin, A. C. T.; Spångberg, D.; Goddard, W. A., III; Hermansson, K. Water Adsorption on Stepped ZnO Surfaces from MD Simulation. *Surf. Sci.* **2010**, *604*, 741–752.
- (40) Rimsza, J. M.; Yeon, J.; van Duin, A. C. T.; Du, J. Water Interactions with Nanoporous Silica: Comparison of ReaxFF and Ab Initio Based Molecular Dynamics Simulations. *J. Phys. Chem. C* **2016**, *120*, 24803–24816.
- (41) Hornak, V.; Abel, R.; Okur, A.; Strockbine, B.; Roitberg, A.; Simmerling, C. Comparison of Multiple Amber Force Fields and Development of Improved Protein Backbone Parameters. *Proteins: Struct., Funct., Bioinf.* **2006**, *65*, 712–725.
- (42) Mortier, W. J.; Ghosh, S. K.; Shankar, S. Electronegativity-Equalization Method for the Calculation of Atomic Charges in Molecules. *J. Am. Chem. Soc.* **1986**, *108*, 4315–4320.
- (43) Chen, J. Charge transfer with polarization current equalization. A fluctuating charge model with correct asymptotics. *Chem. Phys. Lett.* **2007**, *438*, 315–320.
- (44) Broqvist, P.; Kullgren, J.; Wolf, M. J.; van Duin, A. C. T.; Hermansson, K. ReaxFF Force-Field for Ceria Bulk, Surfaces, and Nanoparticles. *J. Phys. Chem. C* **2015**, *119*, 13598–13609.
- (45) Senftle, T. P.; van Duin, A. C. T.; Janik, M. J. Methane Activation at the Pd/CeO₂ Interface. *ACS Catal.* **2017**, *7*, 327–332.
- (46) Kim, B.-H.; Kullgren, J.; Wolf, M. J.; Hermansson, K.; Broqvist, P. Multiscale Modeling of Agglomerated Ceria Nanoparticles: Interface Stability and Oxygen Vacancy Formation. *Front. Chem.* **2019**, *7*, 203.
- (47) Barcaro, G.; Sementa, L.; Monti, S.; Carravetta, V.; Broqvist, P.; Kullgren, J.; Hermansson, K. Dynamical and Structural Characterization of the Adsorption of Fluorinated Alkane Chains onto CeO₂. *J. Phys. Chem. C* **2018**, *122*, 23405–23413.
- (48) Zhang, W.; van Duin, A. C. T. Second-Generation ReaxFF Water Force Field: Improvements in the Description of Water Density and OH-Anion Diffusion. *J. Phys. Chem. B* **2017**, *121*, 6021–6032.
- (49) Adamo, C.; Barone, V. Toward Reliable Density Functional Methods without Adjustable Parameters: The PBE0 Model. *J. Chem. Phys.* **1999**, *110*, 6158–6170.
- (50) *Handbook on the Physics and Chemistry of Rare Earths*; Gschneidner, K. A., Eyring, L., Eds.; North-Holland ; sole distributors for the U.S.A. and Canada, Elsevier North-Holland: Amsterdam ; New York : New York, NY, USA, 1978.
- (51) Greiner, J. D.; McMasters, O. D.; Smith, J. F. Single-Crystal Elastic Constants of γ -Cerium. *Scripta Metallurgica* **1980**, *14*, 989–991.
- (52) Zinkevich, M.; Djurovic, D.; Aldinger, F. Thermodynamic Modelling of the Cerium–Oxygen System. *Solid State Ionics* **2006**, *177*, 989–1001.
- (53) Dovesi, R.; Erba, A.; Orlando, R.; Zicovich-Wilson, C. M.; Civalleri, B.; Maschio, L.; Rérat, M.; Casassa, S.; Baima, J.; Salustro, S.; Kirtman, B. Quantum-Mechanical Condensed Matter Simulations with CRYSTAL. *WIREs Comput. Mol. Sci.* **2018**, No. e1360.
- (54) Da Silva, J. L. F.; Ganduglia-Pirovano, M. V.; Sauer, J.; Bayer, V.; Kresse, G. Hybrid Functionals Applied to Rare-Earth Oxides: The Example of Ceria. *Phys. Rev. B* **2007**, *75*, No. 045121.
- (55) Kullgren, J.; Castleton, C. W. M.; Müller, C.; Ramo, D. M.; Hermansson, K. B3LYP Calculations of Cerium Oxides. *J. Chem. Phys.* **2010**, *132*, No. 054110.
- (56) Graciani, J.; Márquez, A. M.; Plata, J. J.; Ortega, Y.; Hernández, N. C.; Meyer, A.; Zicovich-Wilson, C. M.; Sanz, J. F. Comparative Study on the Performance of Hybrid DFT Functionals in Highly Correlated Oxides: The Case of CeO₂ and Ce₂O₃. *J. Chem. Theory Comput.* **2011**, *7*, 56–65.
- (57) Désaunay, T.; Ringuedé, A.; Cassir, M.; Labat, F.; Adamo, C. Modeling Basic Components of Solid Oxide Fuel Cells Using Density Functional Theory: Bulk and Surface Properties of CeO₂. *Surf. Sci.* **2012**, *606*, 305–311.
- (58) Evarestov, R. A.; Gryaznov, D.; Arrigoni, M.; Kotomin, E. A.; Chesnokov, A.; Maier, J. Use of Site Symmetry in Supercell Models of Defective Crystals: Polarons in CeO₂. *Phys. Chem. Chem. Phys.* **2017**, *19*, 8340–8348.
- (59) Brugnoli, L.; Ferrari, A. M.; Civalleri, B.; Pedone, A.; Menziani, M. C. Assessment of Density Functional Approximations for Highly Correlated Oxides: The Case of CeO₂ and Ce₂O₃. *J. Chem. Theory Comput.* **2018**, *14*, 4914–4927.
- (60) El-Kelany, K. E.; Ravoux, C.; Desmarais, J. K.; Cortona, P.; Pan, Y.; Tse, J. S.; Erba, A. Spin Localization, Magnetic Ordering, and Electronic Properties of Strongly Correlated Ln₂O₃ Sesquioxides (Ln=La, Ce, Pr, Nd). *Phys. Rev. B* **2018**, *97*, 245118.
- (61) Grimme, S. Semiempirical GGA-Type Density Functional Constructed with a Long-Range Dispersion Correction. *J. Comput. Chem.* **2006**, *27*, 1787–1799.
- (62) Brugnoli, L.; Pedone, A.; Menziani, M. C.; Adamo, C.; Labat, F. H₂ Dissociation and Water Evolution on Silver-Decorated CeO₂(111): A Hybrid Density Functional Theory Investigation. *J. Phys. Chem. C* **2019**, *123*, 25668–25679.
- (63) Brugnoli, L.; Pedone, A.; Menziani, M. C.; Adamo, C.; Labat, F. O₂ Activation over Ag-Decorated CeO₂(111) and TiO₂(110) Surfaces: A Theoretical Comparative Investigation. *J. Phys. Chem. C* **2020**, *124*, 25917–25930.
- (64) Dolg, M.; Stoll, H.; Preuss, H. Energy-adjusted Pseudopotentials for the Rare Earth Elements. *J. Chem. Phys.* **1989**, *90*, 1730–1734.
- (65) Graciani, J.; Márquez, A. M.; Plata, J. J.; Ortega, Y.; Hernández, N. C.; Meyer, A.; Zicovich-Wilson, C. M.; Sanz, J. F. Comparative Study on the Performance of Hybrid DFT Functionals in Highly Correlated Oxides: The Case of CeO₂ and Ce₂O₃. *J. Chem. Theory Comput.* **2011**, *7*, 56–65.

- (66) Thakkar, A. J.; Koga, T.; Saito, M.; Hoffmeyer, R. E. Double and Quadruple Zeta Contracted Gaussian Basis Sets for Hydrogen through Neon. *Int. J. Quantum Chem.* **1993**, *48*, 343–354.
- (67) Peintinger, M. F.; Oliveira, D. V.; Bredow, T. Consistent Gaussian Basis Sets of Triple-Zeta Valence with Polarization Quality for Solid-State Calculations. *J. Comput. Chem.* **2013**, *34*, 451–459.
- (68) Monkhorst, H. J.; Pack, J. D. Special Points for Brillouin-Zone Integrations. *Phys. Rev. B* **1976**, *13*, 5188–5192.
- (69) Towler, M. D.; Zupan, A.; Causà, M. Density Functional Theory in Periodic Systems Using Local Gaussian Basis Sets. *Comput. Phys. Commun.* **1996**, *98*, 181–205.
- (70) Dovesi, R.; Saunders, V. R.; Roetti, C.; Orlando, R.; Zicovich-Wilson, C. M.; Pascale, F.; Civalleri, B.; Doll, K.; Harrison, N. M.; Bush, I. J.; D'Arco, P.; Llunell, M.; Causà, M.; Noël, Y.; Maschio, L.; Erba, A.; Rerat, M.; Casassa, S. *CRYSTAL17 User's Manual*; (University of Torino: Torino, 2017). 2017.
- (71) Gale, J. D. GULP: A Computer Program for the Symmetry-Adapted Simulation of Solids. *J. Chem. Soc., Faraday Trans.* **1997**, *93*, 629–637.
- (72) Gale, J. D.; Rohl, A. L. The General Utility Lattice Program (GULP). *Mol. Simul.* **2003**, *29*, 291–341.
- (73) Shanno, D. F. Conditioning of Quasi-Newton Methods for Function Minimization. *Math. Comput.* **1970**, *24*, 647–656.
- (74) Gale, J. D. Empirical Potential Derivation for Ionic Materials. *Phil. Mag. B* **1996**, *73*, 3–19.
- (75) Merinov, B. V.; Mueller, J. E.; van Duin, A. C. T.; An, Q.; Goddard, W. A., III ReaxFF Reactive Force-Field Modeling of the Triple-Phase Boundary in a Solid Oxide Fuel Cell. *J. Phys. Chem. Lett.* **2014**, *5*, 4039–4043.
- (76) Kim, S.-Y.; Kumar, N.; Persson, P.; Sofo, J.; van Duin, A. C. T.; Kubicki, J. D. Development of a ReaxFF Reactive Force Field for Titanium Dioxide/Water Systems. *Langmuir* **2013**, *29*, 7838–7846.
- (77) Swope, W. C.; Andersen, H. C.; Berens, P. H.; Wilson, K. R. A Computer Simulation Method for the Calculation of Equilibrium Constants for the Formation of Physical Clusters of Molecules: Application to Small Water Clusters. *J. Chem. Phys.* **1982**, *76*, 637–649.
- (78) Nosé, S. A Unified Formulation of the Constant Temperature Molecular Dynamics Methods. *J. Chem. Phys.* **1984**, *81*, 511–519.
- (79) Furman, D.; Wales, D. J. Transforming the Accuracy and Numerical Stability of ReaxFF Reactive Force Fields. *J. Phys. Chem. Lett.* **2019**, *10*, 7215–7223.
- (80) Ganduglia-Pirovano, M. V.; Da Silva, J. L. F.; Sauer, J. Density-Functional Calculations of the Structure of Near-Surface Oxygen Vacancies and Electron Localization on CeO₂ (111). *Phys. Rev. Lett.* **2009**, *102*, No. 026101.
- (81) Li, H. Y.; Wang, H. F.; Gong, X. Q.; Guo, Y. L.; Guo, Y.; Lu, G.; Hu, P. Multiple Configurations of the Two Excess 4f Electrons on Defective CeO₂ (111): Origin and Implications. *Phys. Rev. B* **2009**, *79*, 193401.
- (82) Yang, C.; Yu, X.; Heißler, S.; Weidler, P. G.; Nefedov, A.; Wang, Y.; Wöll, C.; Kropp, T.; Paier, J.; Sauer, J. O₂ Activation on Ceria Catalysts—The Importance of Substrate Crystallographic Orientation. *Angew. Chem., Int. Ed.* **2017**, *56*, 16399–16404.
- (83) Jónsson, H.; Mills, G.; Jacobsen, K. W. Nudged Elastic Band Method for Finding Minimum Energy Paths of Transitions. In *Classical and quantum dynamics in condensed phase simulations*; World Scientific, 1998; pp. 385–404.
- (84) Haynes, W. M. *CRC Handbook of Chemistry and Physics*; CRC Press, 2014, 2643.
- (85) McHargue, G. J.; Yakel, H. L., Jr. Phase Transformations in Cerium. *Acta Metall.* **1960**, *8*, 637–646.
- (86) Beaudry, B. J.; Palmer, P. E. The Lattice Parameters of La, Ce, Pr, Nd, Sm, Eu and Yb. *Journal of the Less Common Metals* **1974**, *34*, 225–231.
- (87) Spedding, F. H.; Hanak, J. J.; Daane, A. H. High Temperature Allotropy and Thermal Expansion of the Rare-Earth Metals. *J. Less-Common Met.* **1961**, *3*, 110–124.
- (88) Nakajima, A.; Shin, S.; Kawahara, I.; Ishigame, M. Local-Hopping Mechanism of the O₂-Vacancy in Stabilized ZrO₂ Studied by Measuring the Integrated Intensity of Quasieleastic Light Scattering. *Phys. Rev. B* **1994**, *49*, 14949.
- (89) Rossignol, S.; Gérard, F.; Mesnard, D.; Kappensteine, C.; Duprez, D. Structural Changes of Ce–Pr–O Oxides in Hydrogen: A Study by in Situ X-Ray Diffraction and Raman Spectroscopy. *J. Mater. Chem.* **2003**, *13*, 3017–3020.
- (90) Voloshina, E.; Paulus, B. Influence of Electronic Correlations on the Ground-State Properties of Cerium Dioxide. *J. Chem. Phys.* **2006**, *124*, 234711.
- (91) Bärnighausen, H.; Schiller, G. The Crystal Structure of A-CeO₃. *Journal of the Less Common Metals* **1985**, *110*, 385–390.
- (92) Lipp, M. J.; Jeffries, J. R.; Cynn, H.; Park Klepeis, J.-H.; Evans, W. J.; Mortensen, D. R.; Seidler, G. T.; Xiao, Y.; Chow, P. Comparison of the High-Pressure Behavior of the Cerium Oxides Ce₂O₃ and CeO₂. *Phys. Rev. B* **2016**, *93*, No. 064106.
- (93) Herzberg, G.; Spinks, J. W. T. Spectra of diatomic molecules *Molecular Spectra and Molecular Structure: Diatomic Molecules*; Van Nostrand, 1950; Vol. 1.
- (94) Bishop, S. R.; Duncan, K. L.; Wachsman, E. D. Defect Equilibria and Chemical Expansion in Non-Stoichiometric Undoped and Gadolinium-Doped Cerium Oxide. *Electrochim. Acta* **2009**, *54*, 1436–1443.